

Supporting information for: Active foundering of a continental arc root beneath the southern Sierra Nevada, California

George Zandt, Hersh Gilbert, Thomas J. Owens, Mihai Ducea, Jason Saleeby & Craig H. Jones

Two-part removal

A significant portion of the Sierra Nevada–Mojave Desert batholithic root has been removed by two different mechanisms during two separate time periods. The batholithic root beneath the southernmost end of the Sierra Nevada and its southward extension into the Mojave Desert region were sheared off eastward by a shallow segment of the Laramide flat slab^{1,2}. Saleeby² suggested the Laramide slab was segmented into a shallow flat segment to the south of today's Garlock fault and a deeper flat segment to the north. The northern deeper segment left most of the Sierra Nevada residual root intact until the northward migrating triple junction between the Pacific, Farallon, and North American plates removed the subducting plate from beneath the southern Sierra Nevada sometime between ~20 and 10 Ma (ref. 3). Subsequent mid-Miocene volcanism entrained fragments of the pyroxenite root, showing that it survived subduction⁴⁻⁶. The complete detachment of the batholithic root from the surrounding lithosphere occurred well after subduction ceased, and the detachment was not completed until Pliocene time. Xenoliths in the Pliocene and Quaternary volcanics contain no sign of the pyroxenite mass; instead, those from depths comparable to that of the pyroxenite mass are peridotites that retain evidence of hot emplacement⁴⁻⁶. A high-wavespeed body in the mantle under the southwestern Sierra Nevada and southeastern San Joaquin Valley likely represents either the root itself or a downwelling induced by foundering of the root^{7,8} (Fig. S1).

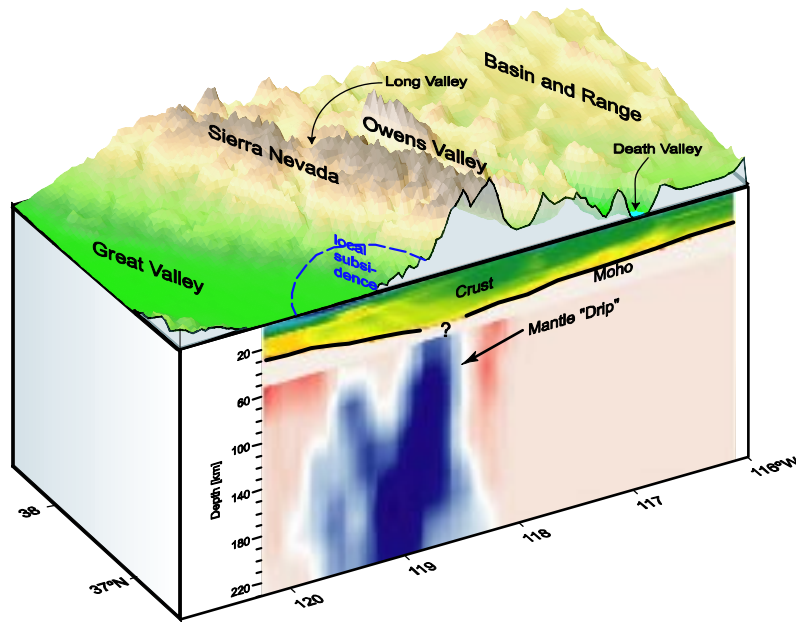


Figure S1 Perspective view of a 3D topographic swath across the Great Valley, Sierra Nevada, Owens Valley, and adjacent Basin and Range. Front panel (from ref. 7) illustrates a 2D cross section combining a crustal velocity model (above 60 km, green is low velocity and yellow is high velocity) and an upper-mantle seismic tomographic image (below 60 km, blue is high velocity and red is low velocity). A localized zone of crustal thickening appears to be associated with the top of a zone of mantle ‘drip’. The intervening zone marked with ‘?’ is not well resolved in past seismic studies but is the focus of this study.

Crustal anisotropy

Receiver functions recorded at many of the stations display directional variations on the radial component as well as significant energy on the transverse component. Factors contributing to these arrivals could be the presence of anisotropic material, dipping layers, scattering, or more complex lateral variations. Observing how the timing and amplitude of phases on the radial and transverse receiver functions vary with direction provides information about which factor contributes to the observed pattern (e.g., refs 9, 10). One example of the azimuthal variations that result from the presence of anisotropy is displayed in the radial and tangential receiver functions shown in Fig. S2. In this plot the observed radial and tangential receiver functions for station JUN are compared to synthetic receiver functions calculated for an anisotropic model with a slow axis of symmetry trending at 270° and plunging 60° (fabric is dipping 30°E). Prominent arrivals in both the observed and synthetic receiver functions on the radial component

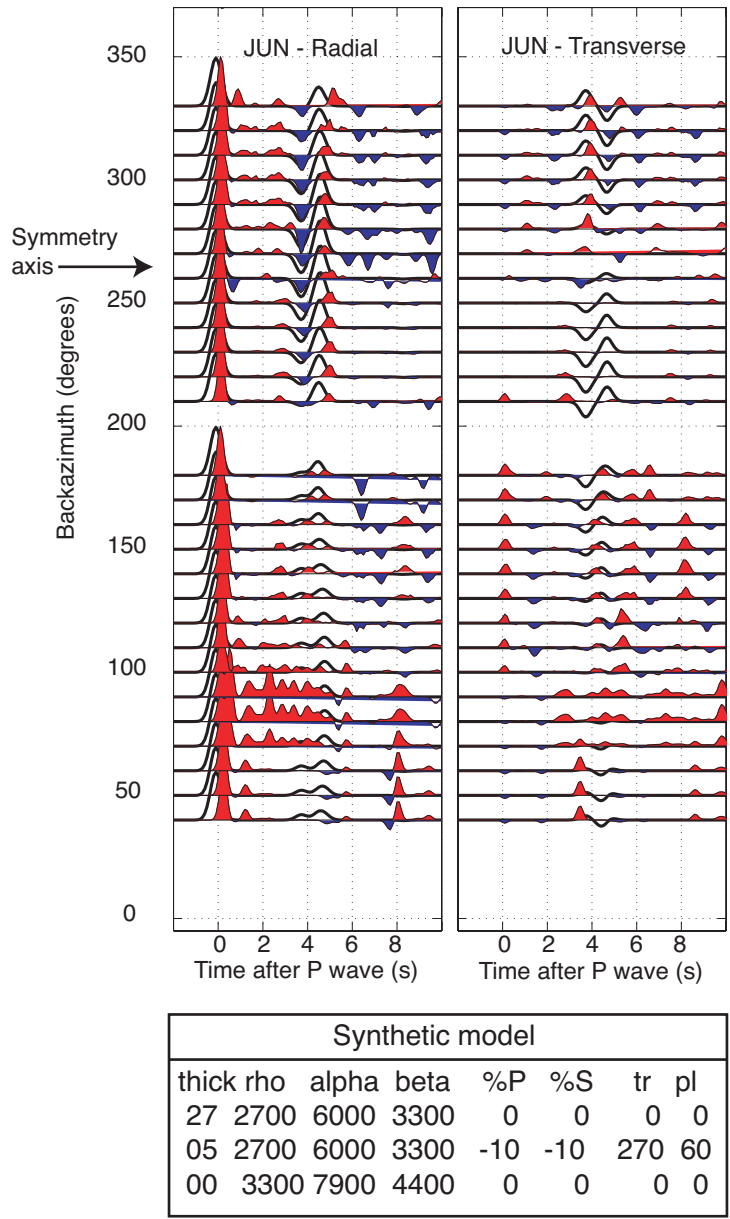


Figure S2 Receiver functions for station JUN stacked into backazimuth bins (red is positive amplitude and blue is negative amplitude) compared to synthetic data (unfilled black lines) for a crustal model with a 5-km-thick, 10% anisotropic layer at the base of the crust. The effect of the anisotropic layer can be observed in the amplitude and polarity variations for the phases arriving between 3 and 5 s on both the radial and transverse components. For an isotropic model, these phases would have constant amplitude on the radial component and no amplitude on the transverse component. The symmetry axis is constrained by the backazimuth, where the largest negative-polarity phases occur on the radial component and the polarity reversals occur on the transverse component.

that lead us to favor this model are the negative-positive pair that arrives prior to 4 s after the *P* wave between backazimuths $\sim 200^\circ$ and 330° and the polarization reversal (negative to positive

going clockwise) on the tangential component near this same direction (Fig. S2). Also important is the diminished amount of energy on both the observed and synthetic receiver functions between $\sim 40^\circ$ and 180° . We find that in comparing various models to data from our stations that models with a slow axis of symmetry plunging at some amount greater than $\sim 45^\circ$ downward to the west provide the best fit to our data. The angle at which the symmetry axis is plunging is not well constrained, but the presence of the plunging axis is required by the data.

Crustal imaging resolution

We migrated and stacked receiver functions calculated from teleseismic recordings in common conversion area bins. Receiver functions ray paths are calculated relative to a grid of stacking bins by assuming a constant V_P of 6.2 km/s and a V_P/V_S of 1.85. The bins are spaced 15 km apart and have a radius of 30 km. The amplitude contribution of receiver functions to each bin is done in a linear manner such that traces along the edges of a bin are weighted by half as much as traces in the center. We test the resolution of the common-conversion-point stacking technique we employed by determining whether or not we are able to resolve features with dips or steps with coarsely spaced stations. We perform this test by computing synthetic receiver functions using a finite-difference algorithm (O. Boyd, personal communication, 2004) for various structures. The station spacing and incidence angles of events we use in the synthetic tests are chosen to reflect those of the actual data. To facilitate comparison between synthetic tests and our observations, we use the same stacking parameters in the tests as in the actual data. We investigated a series of models (Fig. S3, labeled ‘Two steps’, ‘Four steps’, and ‘Constant dip’), each of which has a dipping Moho overlain by a low-velocity zone. The depth to the Moho in each of these models increases by 15 km over 125 km distance ($\sim 7^\circ$ dip), similar to that observed in our data. The shallower low-velocity zone (LVZ) in each of these models dips more gradually (deepening by 10 km over 125 km, $\sim 5^\circ$ dip), being continuous in the continuous-dip model but divided into two and four steps in the step models. These models are designed to determine if the dipping Moho can be resolved and if dipping layers can be differentiated from step-like

features. We recover the dipping Moho in each model, but observe that the pulse shape of the Moho arrival broadens as the LVZ thickens. Differentiation between a continuously dipping LVZ and an LVZ offset by a large step appears possible, as the stacks of the two-step model show distinct, nearly flat negative arrivals that are offset in depth, while the continuous LVZ

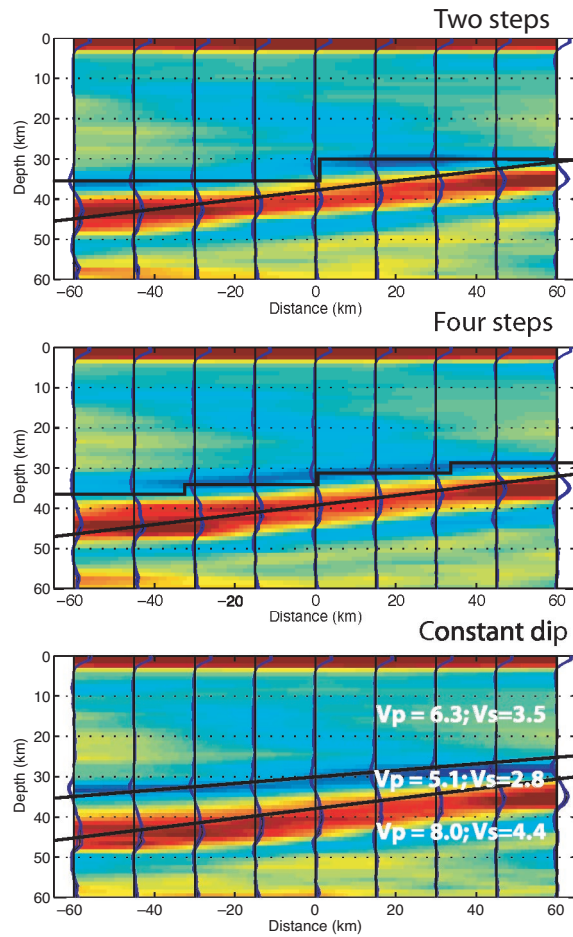


Figure S3 Synthetic stacked receiver function cross sections generated with a finite-difference wave-propagation technique for the seismic model shown beneath the images. The synthetic data were processed with station and bin spacings similar to those used with the Southern Sierra Nevada data.

appears continuous. However, the four-step model illustrates how smaller steps may appear as a continuously dipping layer.

Alternate shear zone interpretation

Fig. S4 illustrates two models that could lead to the anisotropic fabrics observed near the crust-mantle boundary. The observed anisotropy is due either to alignment of slow-axis minerals, such as mica (Fig. 4a, main article), or to fluid- or melt-filled cracks in planes perpendicular to the axis direction (Fig. 4b, main article). In both cases the planes containing the minerals or cracks dip E to NE. The distinction between these two origins for the anisotropy is important because

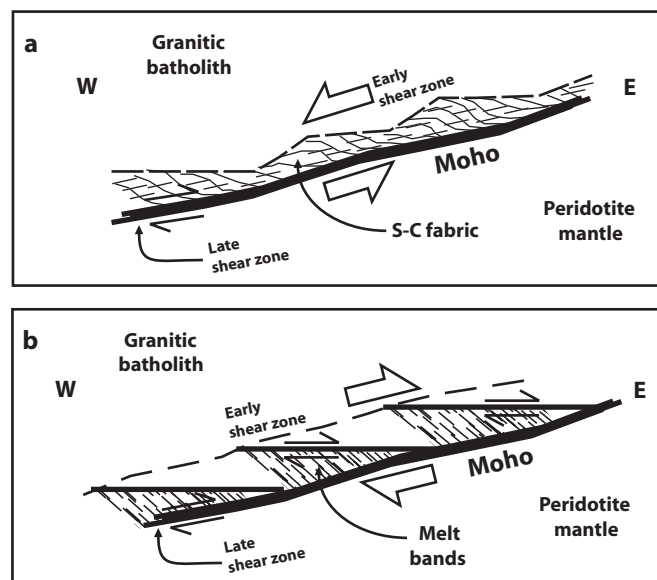


Figure S4 Two possible interpretations are shown for the origin of lower-crustal anisotropy beneath the southern Sierra Nevada. **a**, S-C fabric developed during the early stages of a bottom-to-the-east shear zone. S-C fabrics consist of two sets of planes: S-surfaces are foliation planes that lean over in the direction of shear, and C-surfaces are discrete zones of high shear that align parallel to the shear zone and crosscut the S-surfaces¹⁴. Micas are often concentrated in the S-surfaces and can produce significant seismic anisotropy. This interpretation requires a later reversal in the sense of slip to accommodate the eventual bottom-to-the-west motion of the ultramafic root. **b**, An alternative interpretation is that the anisotropy reflects fluid- or melt-filled fractures that develop during the early stages of a bottom-to-the-west shear zone. The orientation of such fractures is antithetic to the direction of shear. The en echelon relationships of the tops of the anisotropic zones are similar to those of Reidel shears in a later-stage, through-going shear zone¹⁴. This interpretation requires either the release of fluids or partial melting to permit the formation of fractures in the deep crust.

they predict opposite sense of shear with the same alignment (Fig. S4a, b). If the anisotropy is due to oriented micas, the fabric is probably controlled by the development of an S-C fabric (Fig. S4a), and the observed orientation of the anisotropy indicates top-to-the-west shear¹¹, the

opposite sense of the root moving westward into the drip (top-to-the-east sense of shear). These observations can be reconciled by a two-stage evolution. The S-C fabric may have formed in an earlier period, either during Laramide shortening if the shear zone rooted into the mantle, or during an early extensional phase (Fig. 4b, main article) along low-angle detachment faults^{12,13}. This may have initiated the basal shear zone, consistent with the association of S-C fabrics with brittle-ductile deformation in the early, low-strain stages of shear-zone development, but motion on it must have reversed in order to accommodate the eventual westward drip of the root (Fig. 4c, main article). In this model the westward slip must have been confined to a narrower shear zone that did not overprint the early-stage fabric (Fig. S4a).

References

1. Malin, P. E. *et al.* Significance of seismic reflections beneath a tilted exposure of deep continental crust, Tehachapi Mountains, California. *J. Geophys. Res.* **100**, 2069–2087 (1995).
2. Saleeby, J. B. Segmentation of the Laramide slab – Evidence from the southern Sierra Nevada region. *Geol. Soc. Am. Bull.* **115**(6), 655–668 (2003).
3. Atwater, T. & Stock, J. Pacific-North America plate tectonics of the Neogene southwestern United States: An update. *Int. Geol. Rev.* **40**, 575–402 (1998).
4. Ducea, M. N. & Saleeby, J. B. Buoyancy sources for a large, unrooted mountain range, the Sierra Nevada, California: Evidence from xenolith thermobarometry. *J. Geophys. Res.* **101**, 8229–8244 (1996).
5. Ducea, M. N. & Saleeby, J. B. A case for delamination of the deep batholithic crust beneath the Sierra Nevada, California. *Int. Geol. Rev.* **40**, 78–93 (1998).
6. Ducea, M. N. & Saleeby, J. B. The age and origin of a thick mafic-ultramafic keel from beneath the Sierra Nevada batholith. *Contrib. Min. Petrol.* **133**(1-2), 169–185 (1998).
7. Ruppert, S., Fliedner, M. & Zandt, G. Thin crust and active upper mantle beneath the Southern Sierra Nevada in the western United States. *Tectonophysics* **286**, 237–252 (1998).
8. Zandt, G. The southern Sierra Nevada drip and the mantle wind direction beneath the southwestern United States. *Int. Geol. Rev.* **45**, 213–224 (2003).
9. Levin, V. & Park, J. *P-SH* conversions in a flat-layered medium with anisotropy of arbitrary orientation. *Geophys. J. Int.* **131**(2), 253–266 (1997).
10. Jones, C. H. & Phinney, R. A. Seismic structure of the lithosphere from teleseismic converted arrivals observed at small arrays in the southern Sierra Nevada and vicinity, California. *J. Geophys. Res.* **103**, 10065–10090 (1998).
11. Davis, G. H. & Reynolds, S. J. *Structural Geology of Rocks and Regions*, 2nd Ed. (John Wiley & Sons, New York, 1996).

12. Jones, C. H. & Phinney, R. A. Seismic structure of the lithosphere from teleseismic converted arrivals observed at small arrays in the southern Sierra Nevada and vicinity, California. *J. Geophys. Res.* **103**, 10065–10090 (1998).
13. Wernicke, B. P. Cenozoic extensional tectonics of the U.S. Cordillera, in *The Geology of North America Vol. G-3, The Cordilleran Orogen: Conterminous US*. (eds. Burchfiel, B. C., Lipman, P. W. & Zoback, M. L.) 553–581 (Geological Society of America, Boulder, Colorado, 1992).
14. Dumitru, T. A. Subnormal Cenozoic geothermal gradients in the extinct Sierra Nevada magmatic arc: Consequences of Laramide and post-Laramide shallow-angle subduction. *J. Geophys. Res.* **95**, 4925–4942 (1990).